Chapter 4: Intrinsic Anomalous Hall Conductivity and Topological Hall Effect in Ni_2MnGa Magnetic Shape Memory Alloy

In this chapter, the intrinsic anomalous Hall conductivity (AHC) and topological Hall effect in polycrystalline Ni_2MnGa magnetic shape memory alloy are presented. A detailed analysis of AHC suggests that the intrinsic Berry phase mechanisms play major role in the austenite, premartensite, and martensite phases. The magnitude and temperature insensitivity of maximum value of topological Hall resistivity indicates that THE arises due to the real space Berry curvature induced by topologically protected magnetic skyrmion textures in the martensite and premartensite phase of Ni_2MnGa.

4.1 Introduction

The anomalous Hall effect (AHE) is one of the intriguing phenomena in condensed matter physics [151, 312-314]. In the recent past, AHE has received tremendous attention due to its potentiality as the new generation of conventional electronics in the form of spin-based memory devices for e.g., spintronic devices (magnetic random access memory devices) [151, 156], spin orbitronics devices [157], Hall sensor; as well as in the fundamental physics to detect the Berry phase [161], the spin polarization of current carriers [12]. In the ferromagnetic (FM) materials, the AHE appears in addition to the ordinary Hall effect (OHE), which is proportional to the applied magnetic field and related to the Lorentz force [151, 154, 155]. Earlier, it was believed for a long time that AHE scales with magnetization (i.e., proportional to the magnetization) for FM materials, but later it has been realized that AHE also depends critically on the electronic band structure of the materials [151, 158]. The origin of AHE is the result of the joint interaction of spin-orbit coupling (SOC) and magnetization [151, 154, 155]. There are three basic mechanisms; intrinsic (scattering

independent), skew scattering, and side jump; have been proposed to understand the AHE in the magnetic materials. In magnetic materials, the scattering of conduction electrons with spin-orbit coupled magnetic impurities leads to the scattering-dependent skew scattering and side jump mechanisms to the AHE [151, 163]. The skew scattering and side jump mechanisms have been classified as the extrinsic mechanism [151, 163]. The intrinsic mechanism has first explained by Karplus and Luttinger theory [160]. Subsequently, the intrinsic mechanism is interpreted in the framework of momentum space Berry phase and Berry curvature [161]. The Berry curvature depends on the electronic band structure of the materials and deals with topological aspects of the materials [161]. The Berry curvature acts like a pseudomagnetic field in the momentum space, due to which the conducting electrons gain an anomalous velocity perpendicular to the electric field, thus resulting in the AHE even in the absence of an external magnetic field [162]. Since the discovery of the concept of the Berry curvature, which preserves its topology, the AHE has received vast interest in topological materials [158, 314, 315]. A finite Berry curvature manifests a nonzero AHE, and for a finite Berry curvature, the space inversion symmetry or time reversal symmetry must be broken in a material [151, 158]. Subsequently, it was realized that the intrinsic contribution to the AHE depends on the finite Berry curvature, not only on the magnetization of the material for e.g., large AHE has been observed in the antiferromagnetic Mn_3X (X = Ge, Sn, Ga), which has zero net magnetization but has finite Berry curvature [170, 316, 317]. The scaling relation has been derived between anomalous Hall resistivity (ρ_{xy}) and longitudinal resistivity (ρ_{xx}) for the intrinsic and side jump as $\rho_{xy} \propto {\rho_{xx}}^2$, while $\rho_{xy} \propto \rho_{xx}$ for the skew scattering mechanism [163]. The dominant contribution of the different mechanism to the AHE is still a matter of debate in the different systems and require detailed studies [157, 163].

Apart from AHE, recent years are the witness of another exotic phenomenon known as the topological Hall effect (THE) [164-167]. THE is an extra contribution in the total Hall resistivity in addition to the OHE and AHE. THE arises due to the interaction of conduction electrons with the chiral noncoplanar magnetic spin textures, which are associated with the fictitious magnetic field produced by Berry curvature in real space [158, 167] or momentum space [169]. In case of real space Berry curvature induced THE, the maximum value of topological hall resistivity (ρ_T) remains independent of ρ_{xx} (or temperature) [169, 170], while maximum value to ρ_T depends on ρ_{xx} for the momentum space Berry curvature induced THE [169]. Subsequently, THE turns out as a hallmark of the noncoplanar structures with finite spin chirality for e.g., topologically protected magnetic skyrmions [165-167]. The skyrmions are particles-like textures of magnetic spins in the form of swirling of spins around the unit sphere in the nano-scale [178, 232]. The skyrmions are topologically protected in asense that they are characterized by a topological integer that cannot be changed by a continuous deformation [232]. They received giant interest in recent years towards the development of high-density information carriers, data processing, and memory devices [162, 171-174] due to their unique properties such as the nanometer size, topological stability, and low power consumption (low current density~10^5-10^6 A-m^{-2}) required to drive skyrmions [175-177]. Earlier, the skyrmions were observed in materials having broken inversion symmetry (i.e., noncentrosymmetric) for e.g., B20 magnets like MnSi [178], MnGe [179], FeGe [180], Cu_2OSeO_3 [181], etc. In these noncentrosymmetric materials, skyrmions stabilize due to the competition between Heisenberg exchange interactions and Dzyaloshinskii-Moriya interactions (DMI) [182, 183]. Subsequently, the skyrmions were also observed in the centrosymmetric materials having inversion symmetry [11, 185, 186] for e.g., NiMnGa [187], $La_{2-2x}Sr_{1+2x}Mn_2O_7$ [185], MnPdGa [188], NiI_2 [189], etc. In these centrosymmetric materials, the magnetocrystalline anisotropy

(MCA) plays a critical role in stabilizing the magnetic skyrmions due to the competing magnetic interactions between magnetic anisotropy energy and dipolar interaction energy [11, 185, 187]. THE has been extensively investigated in the noncentrosymmetric B20 magnets [167, 177, 190, 191] and other systems having skyrmions [187, 192] or non-trivial spin textures with finite spin chirality [162, 170].

In the recent past, antiskyrmions stable up to high temperature have been observed in noncentrosymmetric Heusler compounds with D_{2d} crystal symmetry for e.g., Mn_2NiGa [165] and Mn-Pt(Pd/Rh)-Sn [166, 193, 194, 318]. All these Heusler compounds show a large THE associated with the skyrmionic spin textures. Interestingly, skyrmions have also been observed in centrosymmetric Ni_2MnGa Heusler compound [11], which also exhibits magnetic shape memory effect [3, 319] and several other fundamental properties like giant negative magnetoresistance [57, 320, 321], large magnetocaloric effect [322, 323], anomalous Hall effect [149, 150], anomalous Nernst effect [13], etc. The stochiometric Ni_2MnGa magnetic shape memory alloy (MSMA) shows both ferromagnetic (FM) and ferroelastic (martensite and premartensite) phase transitions [63, 104]. Skyrmions have been observed in the martensite phase of single-crystalline Ni_2MnGa MSMA [11]. It has been proposed that twin boundaries in the martensite phase offer geometrical confinements to the magnetic structure, which leads to skyrmions formation even in the absence of field in Ni_2MnGa MSMA [11]. Further, a theoretical study proposed that the skyrmions and skyrmion lattices get stabilized by spatial modulation of magnetic anisotropy in the centrosymmetric FM material like Ni_2MnGa [324]. Therefore, Ni_2MnGa is expected to show THE. Interestingly, THE has been observed in the film form of $Ni_{47.3}Mn_{30.6}Ga_{22.1}$ (composition close to Ni_2MnGa) [149]. However, the authors claimed that THE is not related to the skyrmions in Ni_2MnGa [149]. Their claim was based on topological Hall resistivity's sign, magnitude, and

temperature dependency [149]. Thus, the ongoing discussion suggest that there is a controversy about the presence of skyrmion in Ni_2MnGa MSMA. Apart from the controversy of THE, the mechanism of AHE is also not well understood in these MSMAs [149, 157]. This necessitates a detailed study of Hall effect in Ni_2MnGa MSMA.

The present chapter describes the evidence for the momentum space Berry curvature induced AHE and real space Berry curvature induced THE in the bulk Ni_2MnGa MSMA. The XRD and EDAX characterization confirms the phase purity of the sample. The magnetization and resistivity measurements reveal the structural and magnetic phase transitions. The negative MR was found, which can be understood using the *s*-*d* scattering model [57, 320, 325]. The anomalous Hall study reveals the dominance of the intrinsic Berry phase contribution over the extrinsic skew scattering and side jump mechanism in the austenite, premartensite and martensite phases. The detailed Hall data analysis suggests the absence of THE above the FM T_C. Evidence for the THE is observed in the FM austenite, premartensite, and martensite phases. The temperature independence of maximum value of topological Hall resistivity unleashes real-space Berry curvature induced THE, i.e., attributed to topologically protected magnetic skyrmions in the martensite and premartensite phases. The present findings open a new pathway in the field of centrosymmetric skyrmion host systems, which show magnetic shape memory effect.

4.2 Experimental Section

The polycrystalline ingot with nominal composition Ni_2MnGa was prepared by conventional arc-melting technique [266] under argon atmosphere. The appropriate quantity of each constituent element with at least 99.99% purity was melted several times to get uniform composition. The melt-cast ingot was annealed in a vacuum-sealed quartz ampoule (vacuum ~10^{-6} mbar) at a temperature of 1100 K for three days to achieve further homogeneity and then quenched in the ice-

water mixture. A part of the annealed ingot was crushed into powder using a mortar pestle and sealed in quartz ampoule under the argon atmosphere (first evacuated up to $\sim 10^{-6}$ mbar and then argon filled), followed by annealing at 773 K for overnight to remove the residual stresses, if any, introduced during the grinding [148, 267-269]. This annealed powder sample was used for x-ray diffraction (XRD) measurement using an 18-kW Cu rotating anode-based x-ray diffractometer (Rigaku) equipped with a curved graphite crystal monochromator in the diffraction beam. A rectangular-shaped sample from the annealed ingot was used for all other characterizations. The chemical composition was checked using the energy dispersive analysis of x-rays (EDAX) technique. The EDAX characterization was performed using EVO-Scanning Electron Microscope MA15/18 (ZEISS, SEM) on the different parts of the sample. The average composition so obtained is $Ni_{1.96}Mn_{1.02}Ga_{1.02}$, which is slightly different from that observed in chapter 3(see section 3.2). Hereafter, the present $Ni_{1.96}Mn_{1.02}Ga_{1.02}$ composition will be termed as Ni_2MnGa. The backscattered electron (BSE) images were also recorded for the phase-contrast study.

The longitudinal resistivity (ρ_{xx}) data was collected in cooling and warming cycles with a temperature sweep rate of 2 K/min using Cryogen Free Measurement System (Cryogenic Limited, UK). The magnetization and magneto-transport data were collected using a vibrating sample magnetometer (VSM) module and electrical transport option (ETO) equipped in a Physical Properties Measurement System (PPMS, Quantum Design), respectively. The temperature dependence of dc magnetization (*M(T)*) at an applied magnetic field of 100 Oe was collected in zero-field cooled warming (ZFCW), field cooling (FC), and field cooled warming (FCW) protocols with the temperature sweep rate of 2 K/min. In the ZFCW protocol, the sample was cooled from 400 K (above its ferromagnetic T_C) down to 2 K without a magnetic field. Then the field was applied at 2 K, and after that, magnetization was collected during warming. Further, the

data were also collected while cooling the sample under field (FC) and warming on the field cooled sample (FCW). The isothermal field dependence of magnetization (*M(H)*) data was collected while decreasing the temperature in the 385 K to 2 K range covering all the phase transitions observed in *M(T)*. In the magneto-transport measurements, the electrical current was applied along the length (say x-direction) with applied magnetic field direction orthogonal to the specimen (say z-direction). The ρ_{xx} was measured along the length (parallel to the direction of current), while the transverse (or Hall) resistivity was measured along the width of the specimen (perpendicular to the direction of current). The isothermal longitudinal and transverse resistivity data were collected at similar temperatures where *M(H)* data were collected, in the magnetic field range of -5 to +5 Tesla.

4.3 Results and Discussion

4.3.1 Phase purity

The average crystal structure was refined by the Rietveld technique [298] using powder XRD data. The refinement was performed using the FULLPROF package [299]. All the atoms were considered at special Wyckoff sites i.e., Ni at 8*c* (0.25, 0.25, 0.25) and (0.75, 0.75, 0.75), Mn at 4*a* (0, 0, 0) and Ga at 4*b* (0.5, 0.5, 0.5), for the refinement of the crystal structure of cubic austenite phase in the $Fm\bar{3}m$ space group [63, 85, 104]. Rietveld refinement using XRD data at room temperature of Ni_2MnGa MSMA for cubic austenite phase in the $Fm\bar{3}m$ space group is shown in Figure 4.1, which shows an excellent fit between observed and calculated profiles by accounting for all the Bragg peaks. The refined lattice parameter was found to be 5.8235(1) Å, which is in good agreement with those reported in the literature [13, 104]. An enlarged view of fit in 25 to 33º 2θ-range is shown in the inset (i) of Figure 4.1 wherein the presence of (111) and (200) Bragg reflections confirm the $L2_1$ ordering in the cubic austenite phase [13]. The inset (ii) of Figure 4.1 shows the scanning electron microscope image collected in the backscattered electron mode (i.e., BSE image). The

thin line-like contrast in the BSE image is due to scratches that appeared on the sample during its polishing. Apart from the scratches, the BSE image clearly displays single contrast. Thus, XRD data and BSE image confirm the phase homogeneity of the Ni_2MnGa sample.

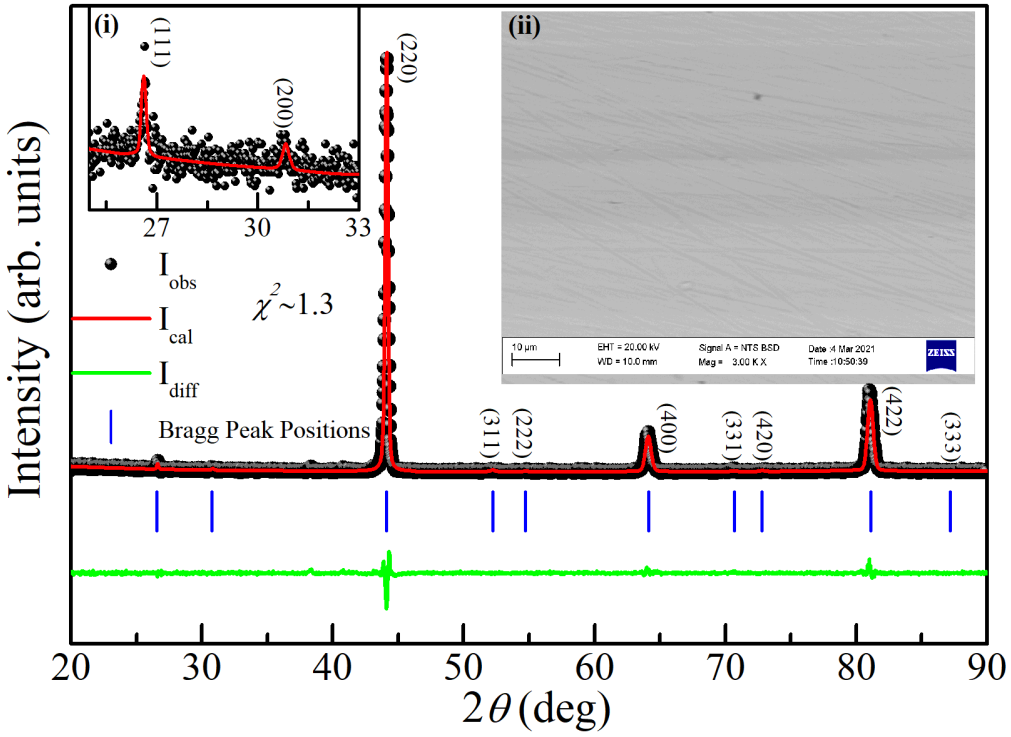

Figure 4.1: The observed (dark black dots), calculated (continuous red line), and difference profiles (green bottom line) obtained after Rietveld refinement of cubic austenite phase in the $Fm\bar{3}m$ space group using x-ray powder diffraction data at room temperature of Ni_2MnGa. Above the difference profile, the vertical tick marks represent the Bragg peak positions whose miller indices are indicated. The inset (i) depicts an enlarged view of the fit at the low 2θ-range. The inset (ii) shows a BSE image of Ni_2MnGa.

4.3.2 Temperature and Magnetic Field Dependent Magnetization

After confirming the phase purity, we now proceed towards the phase transitions of Ni_2MnGa MSMA. The temperature dependence of *M(T)* data measured at 100 Oe under ZFCW, FC and

FCW protocols is shown in Figure 4.2(a). Following the FC cycle, the sharp rise in the magnetization around 380 K is attributed to second-order paramagnetic to ferromagnetic (FM) phase transition. The FM transition temperature was obtained at T_C ~ 377 K by taking minima of the derivative of FC data *w.r.t* temperature. On lowering the temperature further, a small drop in *M(T)* is observed due to cubic austenite to the premartensite phase transition (PMT) with premartensite start temperature $PM_S^C = T_{PM}$ ~ 250 K, where T_{PM}, subscript S, and superscript C correspond to the PMT temperature, "start temperature" of PMT, and "cooling cycle", respectively. Finally, a sharp drop attributes to the premartensite to martensite phase transition (MPT) with martensite start temperature $M_S^C = T_M$ ~ 175 K, where T_M, is the MPT temperature. The drop in magnetization across PMT and MPT is due to higher magnetocrystalline anisotropy energy in comparison to the FM cubic austenite phase [263, 326]. The appearance of different characteristic transition temperatures in FC and FCW cycles across the MPT manifest the thermal hysteresis, which confirms the first-order character of MPT in Ni_2MnGa MSMA [63, 64, 66]. In addition, a small thermal hysteresis across PMT reveals the weakly first-order character of the FM austenite to FM premartensite phase transition [63, 64, 327]. The present *M(T)* behavior is in good agreement with those given in section 3.4.1 of chapter 3. The magnetic behavior of each phase is verified by the magnetic field dependence of magnetization (*M(H)*) measurements in each phase. The *M(H)* in the austenite, premartensite, and martensite phases in the temperature range of 385-2 K is shown in Figure 4.2(b). The *M(H)* data at 385 K, which is close to the onset temperature of FM transition (T_{onset} ~ 381 K, see the inset of Figure 4.2(a)), suggest that the specimen is mainly in the paramagnetic state with a small amount of FM phase present due to fluctuation near T_C. Below 385 K, the saturating tendency of *M(H)* at high field suggests that the specimen reaches in the FM state (Figure 4.2(b)). However, the higher saturation field observed in the martensite phase

compared to the austenite and premartensite phases is certainly due to the presence of strong magnetocrystalline anisotropy in the martensite phase [326] (see Figure 4.2(b)). Therefore, a higher field is required to orient the martensite twin variants (see sections 1.1 and 1.3 for the detailed discussion for twin variants) along the direction of the applied field. The present behavior of *M(T)*, *M(H)*, and transition temperatures are in good agreement with those reported in the literature [13, 63, 148, 305].

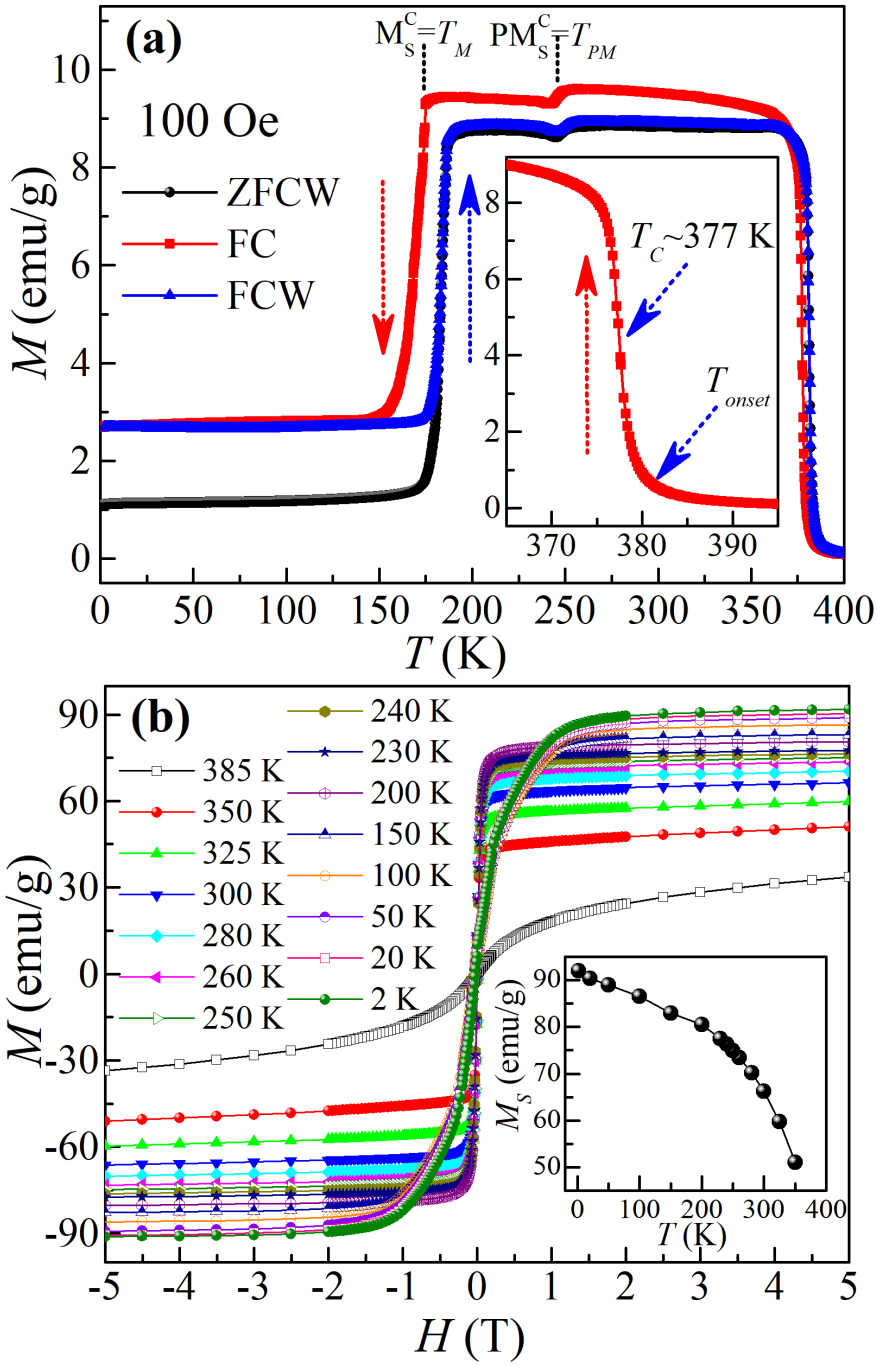

Figure 4.2: (a) Temperature dependence of dc magnetization (M) of Ni_2MnGa, measured at 100 Oe in the zero-field cooled warming (ZFCW; black color), field cooled (FC; red color), and field cooled warming (FCW; blue color) cycles. The inset in (a) depicts an enlarged view around paramagnetic to ferromagnetic transition. The T_M, T_{PM}, T_{onset}, and T_C (indicated in the inset) represent the martensite, premartensite, onset of ferromagnetic, and ferromagnetic transition

temperatures, respectively. The arrows are to guide the cooling and warming cycles. (b) The magnetic field dependence of magnetization of Ni_2MnGa, measured at the indicated temperatures (385-2 K), wherein inset depicts the temperature dependency of the saturation magnetization (M_S).

4.3.3 Resistivity and Magnetoresistance

In addition to the magnetization, the phase transition was also verified by resistivity measurements. The temperature dependence of longitudinal resistivity (ρ_{xx}), measured in the cooling and warming cycles at zero-field and 1 T, is shown in Figure 4.3(a), which shows monotonic metallic behavior. In addition, a sudden rise in ρ_{xx} around 175 K during the cooling cycle and a sharp drop around 185 K during the warming cycle correspond to MPT and reverse MPT, respectively, as depicted in the inset of Figure 4.3(a), which reveals a clear thermal hysteresis across as expected [13]. The rise in ρ_{xx} in the martensite phase is due to the formation of twins with different crystallographic orientation separated by twin boundaries [14]. These twins and twin boundaries serve as the obstacle for the conducting electrons and result in a rise in the value of ρ_{xx} in the martensite phase. Besides MPT, another dip-like behavior observed around temperature 250 K in the ρ_{xx}, as marked by an arrow in Figure 4.3(a). This dip is attributed to the PMT with PMT temperature T_{PM} ~ 250 K. The premartensite phase has been considered as a micromodulated domains with preserved cubic austenite phase symmetry [63, 100, 120, 328]. Therefore, only a small dip appeared in ρ_{xx} across PMT in comparison to sharp change across MPT. It is worth to mention here that the resistivity data at higher field (1 T) reveals the suppression of MPT in agreement with the Clausius-Clapeyron equation [329, 330] while suppression of PMT temperatures due to its magnetoelastic character of PMT [100].

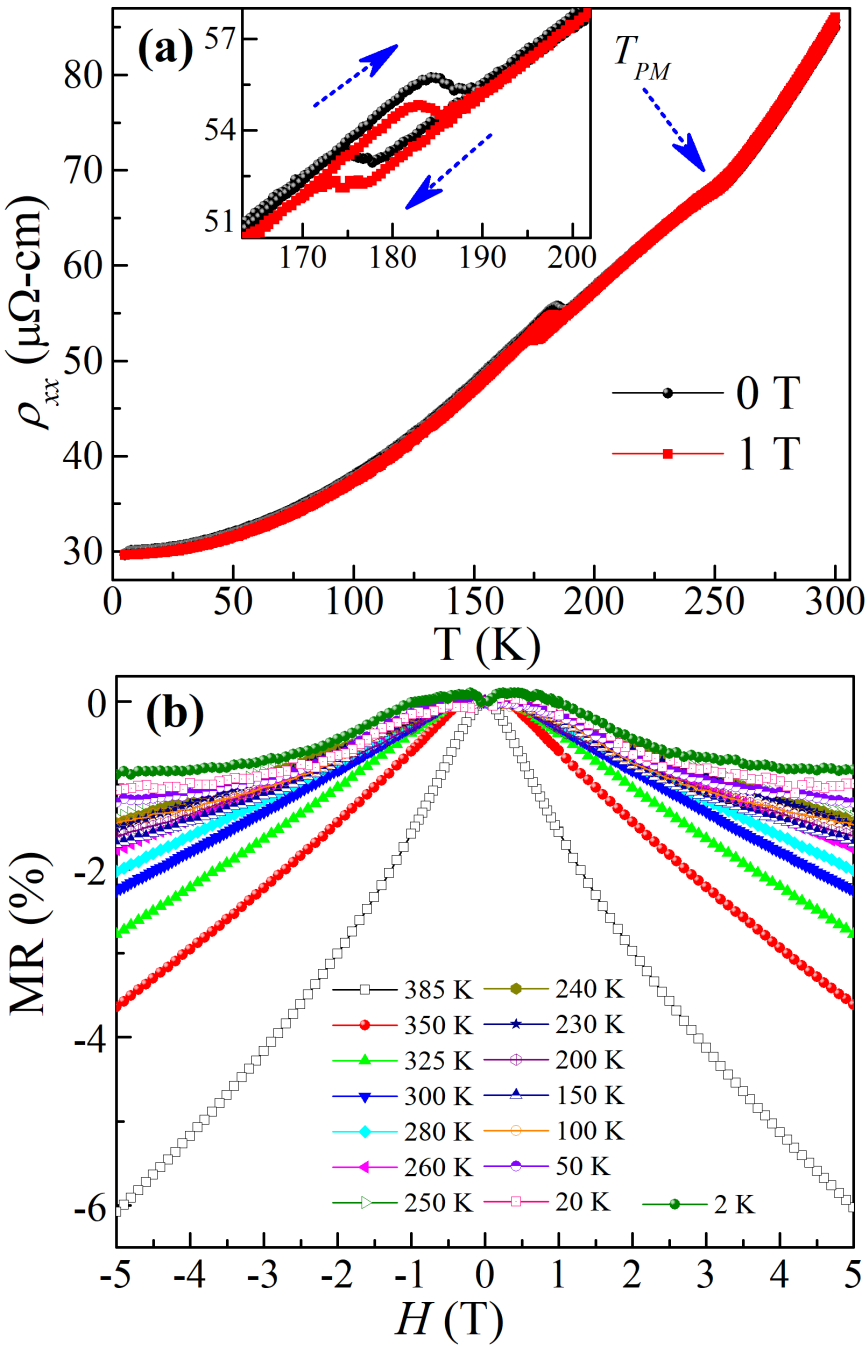

Figure 4.3: (a) Temperature dependence of longitudinal resistivity (ρ_{xx}) of Ni_2MnGa, measured in cooling and warming cycles at 0 and 1 T. The insets depict an enlarged view around the martensite phase transition where cooling and warming cycles are indicated by arrows. The T_{PM} indicates the premartensite transition temperature. (b) The magnetic field dependence of magnetoresistance (MR) of Ni_2MnGa, measured at the indicated temperatures (385-2 K).

The magnetoresistance (MR) measurements were carried out for the detailed Hall study (given in section 4.3.4). The MR was calculated using the equation MR (%) = $\{((\rho_H - \rho_0)/\rho_0)\times 100\}$, where ρ_H and ρ_0 are longitudinal resistivity at any magnetic field *H* and zero-field, respectively [57, 320, 325]. The magnetic field dependence of percentage MR in the austenite, premartensite, and martensite phases at the different temperatures in the 385-2 K range is shown in Figure 4.3(b), which demonstrates the presence of negative MR in agreement with those reported in the literature [57, 320, 325]. The appearance of negative MR in Ni-Mn-Ga MSMAs has been explained using the *s*-*d* scattering model where scattering is considered between conduction electron of *s*-orbital with the localized *d*-spins of magnetic elements [57, 320, 325]. The application of the magnetic field tends to align the magnetic domains of *d*-spins. This causes a reduction in the *s*-*d* scattering and results in negative MR [325]. The net change in magnitude of the negative MR with magnetic field decreases on decreasing the temperature for e.g., negative MR is around ~6 % at 385 K (paramagnetic austenite phase), ~3.7 % at 350 K (FM austenite phase), while it reduces to around ~1 % at 2 K (FM martensite phase) at $\pm$5 T (Figure 4.3(b)). The relatively smaller change in MR at lower temperatures in comparison to higher is due to the reduction in the *s*-*d* scattering at lower temperatures [325]. The behavior of present temperature dependent ρ_{xx} and MR are in good agreement with the literature [13, 320].

4.3.4 Anomalous Hall Effect

Since Ni_2MnGa exhibits magnetostructural phase transition (martensite and premartensite) [331] where electronic band structure changes drastically [13], and AHE also depends on the electronic band structure through the intrinsic mechanism, it is useful to study the AHE to explore the understanding of the mechanism involved in the magnetostructural phase transition. Therefore, we

proceed towards the AHE study in Ni_2MnGa MSMA. The Hall resistivity (ρ_{xy}) was obtained by the anti-symmetrizing the raw Hall resistivity data (ρ_{xy}^{raw}) by averaging the difference of ρ_{xy}^{raw} at the positive and negative applied field to get rid of the longitudinal components, i.e., $\rho_{xy} = \{\rho_{xy}(+H) - \rho_{xy}(-H)\}/2$. The ordinary Hall contribution was removed from the ρ_{xy} to obtain the actual transverse resistivity corresponding to the anomalous Hall effect (ρ_{AHE}) by the method discussed as follows.

The expression for the ρ_{xy} can be given as [151, 332]:

$$\rho_{xy} = R_0 H + R_S M \ldots (4.1),$$

where, $R_0 H$ and $R_S M$ (or ρ_{AHE}) are the resistivities corresponding to the ordinary and anomalous Hall effect, respectively. Further, the R_0, R_S, H, and M are ordinary Hall coefficient, anomalous Hall coefficient, applied magnetic field, and magnetization, respectively. Fitting of experimental ρ_{xy} with field using eq. (4.1) (i.e., equation of line) at higher field region provides the value of slope (R_0). To calculate the ρ_{AHE} with the magnetic field, ordinary Hall contribution was subtracted from the ρ_{xy} by using the obtained value of R_0 i.e., $\rho_{AHE} = \rho_{xy} - R_0 H$. The ρ_{AHE} in the temperature range of 385-2 K is shown in Figure 4.4(a), which reveals that the behavior of ρ_{AHE} is analogous to the *M(H)* i.e., saturating tendency at higher field. This is due to the fact that the ρ_{AHE} scales with the magnetization, which is the key feature of AHE in the FM systems like Ni_2MnGa.

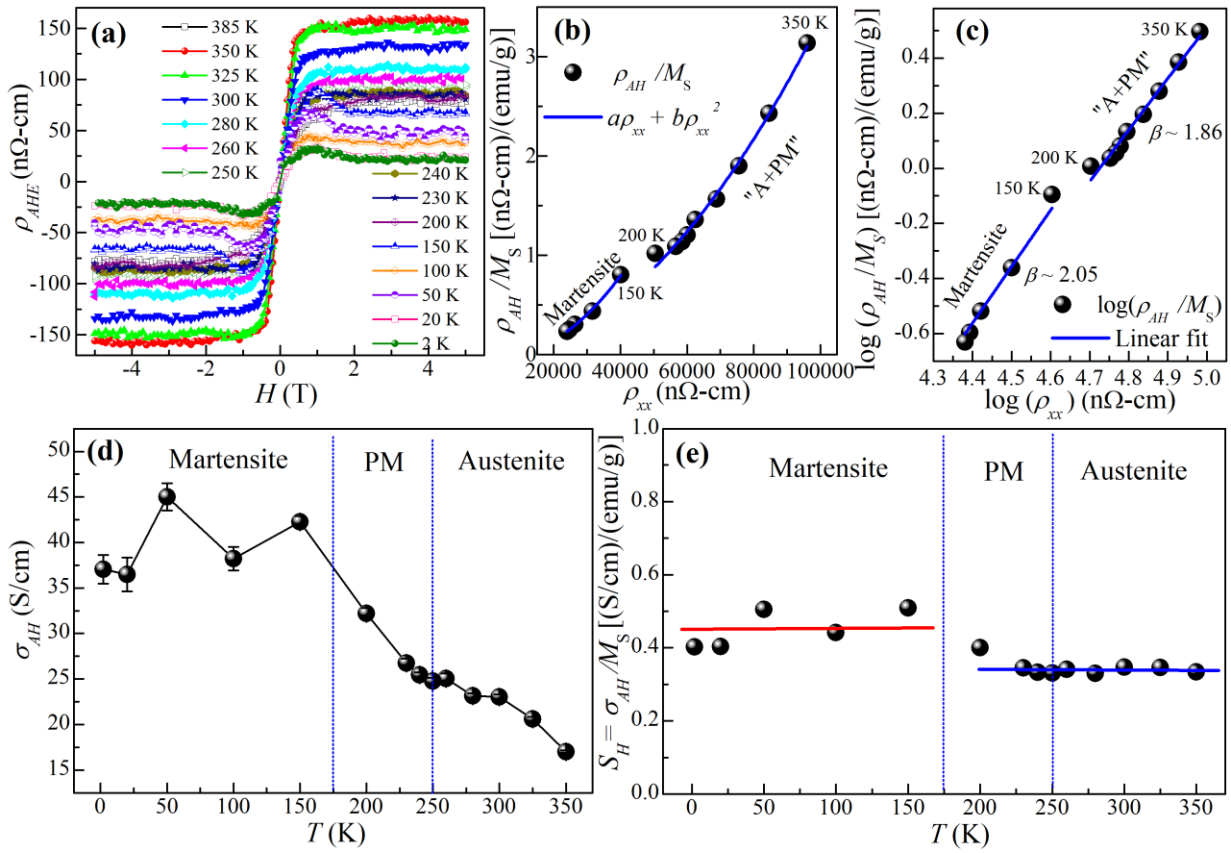

Figure 4.4: (a) The magnetic field dependence of resistivity corresponding to the anomalous Hall effect (ρ_{AHE}) of Ni_2MnGa, measured at the indicated temperatures (385-2 K). (b) Variation of anomalous Hall resistivity divided by saturation magnetization (ρ_{AH}/M_S) with longitudinal resistivity (ρ_{xx}) and (c) their logarithm value (dark black dots) in the martensite and in both austenite and premartensite ("A+PM") phases. The blue line represents in (b) fitting using equation $\rho_{AH}/M_S = a\rho_{xx} + b\rho_{xx}^2$ and (c) linear fit wherein the value of slope (β) of the linear fit is indicated. (d) Temperature dependency of the anomalous Hall conductivity (σ_{AH}). (f) Temperature dependency of scaling coefficient ($S_H = \sigma_{AH}/M_S$), where red and blue line represent the temperature independency of S_H in the martensite and "A+PM" phases, respectively. The austenite, premartensite (PM), and martensite phases are separated by dashed lines in (d) and (f).

The zero-field extrapolation of high field ρ_{AHE} (Figure 4.4(a)) provides the value of anomalous Hall resistivity (ρ_{AH}) at the particular temperature and can be given by equation [151] [314, 332],

$$\rho_{AH} = (a\rho_{xx} + b\rho_{xx}^{2})M_S \ldots (4.2)$$

$$\frac{\rho_{AH}}{M_S} = a\rho_{xx} + b\rho_{xx}^{2} \ldots (4.3)$$

where *a* and *b* are the coefficients related to extrinsic skew scattering and intrinsic together with extrinsic side jump contribution, respectively while M_S indicates the saturation magnetization. Since there are significant changes in the magnetization with temperature change (see the inset of Figure 4.2(b)), the contribution of magnetization is necessary to consider in the eq. (4.2) [314, 333]. In order to find the different contributions of underlying mechanisms involved in the AHE, $\frac{\rho_{AH}}{M_S}$ vs ρ_{xx} plot is fitted using eq. (4.3) as shown in Figure 4.4(b), which clearly shows different slopes in the martensite phase in comparison to the austenite and premartensite ("A+PM") phases. It is noteworthy that a bad fit was observed when all the three phases (austenite, premartensite, and martensite) were considered simultaneously in the fitting. This is certainly due to the fact that "A+PM" phases have almost similar kinds of crystallographic structures (preserved cubic symmetry) [63, 100, 120, 328]. In contrast, the martensite phase exhibits symmetry breaking, which manifests different crystallographic structures with lower symmetry than the cubic austenite phase [104]. The symmetry breaking in the martensite phase attributes to change in the electronic structure [334] and leads to variation in the slope of anomalous Hall resistivity at the phase boundary of the martensite and premartensite phases. Therefore, the fitting was carried out for "A+PM" phases together while separately fitted for the martensite phase. After fitting, we obtained the value of $a \sim 1.14\times10^{-6}$ $(emu/g)^{-1}$ and $b \sim 3.24\times10^{-7}$ $(\mu\Omega\text{-}cm)^{-1}(emu/g)^{-1}$ for the "A+PM" phases, while it is $a \sim -5.45\times10^{-6}$ $(emu/g)^{-1}$ and $b \sim 6.29\times10^{-7}$ $(\mu\Omega\text{-}cm)^{-1}(emu/g)^{-1}$ for the martensite phase. For the martensite phase, the negative sign of *a* suggests that the skew scattering contribution is opposite to both intrinsic and side jump contribution [335]. These values of *a* and

b were used to obtain the different contributions separately in the "A+PM" and martensite phases. The results suggest that intrinsic and side jump contributions ($b\rho_{xx}{}^2 M_S$) is quite larger than the skew scattering contribution ($a\rho_{xx}M_S$) both in the "A+PM" and martensite phases. Further, the $\log(\rho_{AH}/M_S)$ vs $\log(\rho_{xx})$ plot is shown in Figure 4.4(c), which shows the different slope in the martensite phase in comparison to "A+PM" phases, similar to Figure 4.4(b). The linear fitting was carried out to determine the value of exponent β using the scaling relation $\rho_{AH} \propto \rho_{xx}{}^{\beta}$ [333]as shown by blue lines in Figure 4.4(c). If β = 1, the skew scattering dominates, while for β = 2, the intrinsic and/or side jump mechanism dominate in AHE [333, 336]. After fitting, the value of β was found to be ~2.05 in the martensite phase and ~1.86 in the "A+PM" phases. These values of β are close to 2, which suggests that the origin of AHE is governed by intrinsic and/or side jump mechanisms both in the martensite phase and the "A+PM" phases of Ni_2MnGa.

To get more insight about the origin of AHE, it is necessary to look at the behavior of anomalous Hall conductivity (AHC) with temperature (or longitudinal resistivity (ρ_{xx})). In order to obtain that, first of all, Hall conductivity was calculated using the tensor relation given below [315, 333],

$$\sigma_{xy} = \frac{\rho_{xy}}{\rho_{xy}^2+\rho_{xx}^2} \ldots (4.4)$$

The AHC (σ_{AH}) was obtained by zero-field extrapolation of the high field σ_{xy} at the individual temperatures for e.g., σ_{AH} ~ 23 S/cm at room temperature. However, the obtained σ_{AH} merely changes with temperature in the "A+PM" phases, a nearly temperature independent behavior obtained in the martensite phase as shown in Figure 4.4(d). Since the intrinsic AHC (σ_{AH}^{in}) varies proportional to the magnetization, i.e., $\sigma_{AH}^{in} \propto M$, the proportionality or scaling coefficient $S_H = \frac{R_S\mu_0}{\rho_{xx}^2} = \frac{\sigma_{AH}^{in}}{M}$ should be constant and independent of temperature (where, R_S and μ_0 are anomalous Hall coefficient and permeability of free space, respectively) [332, 333]. The obtained value of S_H

as a function of temperature is shown in Figure 4.4(e), which reveals a temperature independent behavior of S_H in the martensite as well as "A+PM" phases. The temperature independent behavior of S_H affirms the dominance of intrinsic Berry phase contribution to the AHC. Out of the total value of AHC, the intrinsic contribution to the AHC, i.e., σ_{AH}^{in} was found to be ~ 21.5 S/cm at 300 K (austenite), ~ 25.1 S/cm at 230 K (premartensite), and ~ 57.9 S/cm at 2 K (martensite) (obtained from Figure 4.4(b)). It is important to mention here that the value of intrinsic AHC in the martensite phase (σ_{AH}^{in} ~ 57.9 S/cm at 2 K) is found to be larger than the value of total AHC (shown in Figure 4.4(d)) because skew scattering mechanism contributes negatively ($a \sim -5.45\times10^{-6}$ (emu/g)$^{-1}$) in the martensite phase. In addition, the longitudinal conductivity ($\sigma_{xx} = 1/\rho_{xx}$) was found to be $\sigma_{xx} \sim 1.3\times10^{4}$ (S/cm) which lie in the moderate conductivity range of $10^4 < \sigma_{xx} < 10^6$ S/cm [165]. This also indicates the dominating intrinsic contribution in the AHC. It is worth mentioning here that the extrinsic side jump contribution to the AHC has been reported to be the order of $\left(\frac{e^2}{ha}\right)\left(\frac{\epsilon_{SO}}{E_F}\right)$, where ϵ_{SO} and E_F are spin-orbit interaction energy and the Fermi energy, respectively [333]. Since, $\frac{\epsilon_{SO}}{E_F}$ is generally less than 0.01 for ferromagnetic metals [332, 333] therefore, the side jump contribution is expected to be very small in these alloys and can be neglected in comparison to the intrinsic contribution to AHC. Thus, intrinsic Berry phase contribution plays major role to the AHC in ferromagnetic Ni_2MnGa. In the martensite phase of Ni_2MnGa, the fermi surface nesting feature manifests the electronic band structure change [90, 337]. This anticipates the dominance of the intrinsic mechanism in the martensite phase as the intrinsic mechanism governed by the electronic band structure of the materials [151]. A recent anomalous Nernst study revealed the significant change in the electronic structure across the modulated premartensite phase transition of Ni_2MnGa [13]. This manifests the dominance of the band structure dictated intrinsic Berry mechanism also in the premartensite phase. Further, we have shown using pair distribution

function study that the modulated premartensite phase presents even in the austenite phase in the short-range region [64]. This anticipates the presence of the intrinsic mechanism to the AHE even in the austenite phase. It is important to note that although the Nernst signal changes significantly across the premartensite phase transition [13], Hall resistivity or Hall conductivity did not change much across premartensite phase transition. This suggests that Hall measurement is less sensitive to capture weak feature of the premartensite phase as compared to the Nernst technique.

4.3.5 Topological Hall Effect

Apart from the anomalous Hall effect, it is interesting to note that there are hump-like features clearly visible at the low field region of the ρ_{AHE} in the martensite phase for e.g., at 150 K around $\pm$1 T of field (Figure 4.4(a)). The hump-like feature in ρ_{AHE} is an indication of extra contribution into the experimental Hall resistivity (ρ_{xy} or ρ_{xy}^{exp}). This extra contribution is a signature of the topological Hall effect (THE) [167, 187, 190], which received tremendous interest in recent years, especially in the skyrmion host systems [232, 338, 339]. This motivated us to go for an investigation of experimental Hall resistivity. The complete expression for total Hall resistivity considering THE is given below [149, 165, 166, 187, 191]:

$$\rho_{xy} = R_0 H + R_S M + \rho_{xy}^{T} \quad \ldots (4.5),$$

where, ρ_{xy}^{T} corresponds to the topological Hall resistivity. As discussed above in section 4.3.4, the intrinsic contribution to the AHE dominates for austenite, premartensite, and martensite phases (see Figure 4.4(e)). Therefore, the skew scattering contribution to AHE can be neglected, and we can take $R_S = b\rho_{xx}^2$ in eq. (4.5). In the high field region, the ρ_{xy}^{T} generally vanishes due to transformation of non-trivial spin structure into the trivial spin structure [187]. Therefore, in the high field region, eq. (4.5) can be rearranged as $\rho_{xy}/H = R_0 + b\rho_{xx}^2 M/H$, who's intercept ($R_0$) and

slope (b) are obtained by linear fitting of ρ_{xy}/H vs $\rho_{xx}^2 M/H$ plot at high field regime [191]. After fitting, the obtained value of R_0 and b are used to obtain the calculated Hall resistivity as $\rho_{xy}^{cal} = R_0 H + b\rho_{xx}^2 M$ for whole field region (low as well as high field). Finally, the difference between ρ_{xy} (or ρ_{xy}^{exp}) and ρ_{xy}^{cal} provides ρ_{xy}^{T} i.e., $\rho_{xy}^{T} = \rho_{xy} - \rho_{xy}^{cal}$. The comparison of ρ_{xy}^{exp} with ρ_{xy}^{cal} is shown in Figure 4.5(a)-(i) at the indicated temperatures.

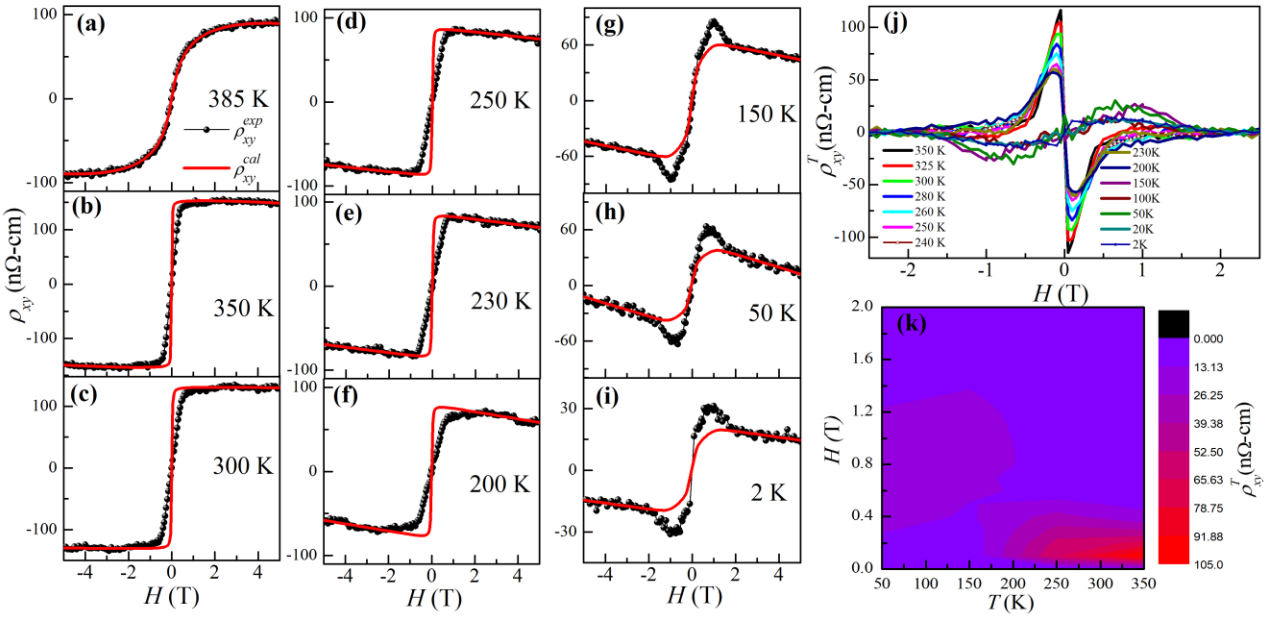

Figure 4.5: The magnetic field dependence of (a)-(i) experimental (ρ_{xy}^{exp}; dark black dots connected with line) and calculated Hall resistivity (ρ_{xy}^{cal}; red continuous line) and (j) topological Hall resistivity (ρ_{xy}^{T}) of Ni_2MnGa at the indicated temperatures. The (k) depicts the contour mapping of the magnitude of ρ_{xy}^{T} as a function of the magnetic field (H) and temperature (T).

The field dependency of ρ_{xy} (or ρ_{xy}^{exp}) and ρ_{xy}^{cal} are depicted in Figure 4.5(a) at 385 K in the austenite phase. At 385 K, the ρ_{xy}^{exp} have saturation tendency at the higher field (Figure 4.5(a)), which is due to AHE emerged by the presence of traces of FM phase appeared by fluctuation even at 385 K, which is close to the onset of FM T_C (inset of Figure 4.2(a)). It is evident from Figure

4.5(a) that the ρ_{xy}^{exp} and ρ_{xy}^{cal} matches perfectly at 385 K, which results the vanishing of THE i.e., $\rho_{xy}^{T} = 0$ at 385 K. On lowering the temperature, the specimen enters in perfectly FM austenite phase, where a slight mismatch between ρ_{xy}^{exp} and ρ_{xy}^{cal} at lower field region clearly observed as shown in Figure 4.5(b) and Figure 4.5(c), at 350 K and 300 K, respectively. This mismatch enhances gradually on further lowering the temperature to the FM premartensite phase (T_{PM} ~ 250 K), as evidenced by the ρ_{xy}^{exp} and ρ_{xy}^{cal} at temperatures 250 K, 230 K and 200 K shown in Figure 4.5(d), Figure 4.5(e) and Figure 4.5(f), respectively. The ρ_{xy}^{exp} and ρ_{xy}^{cal}, in the FM martensite phase (T_M ~ 175 K), at temperatures 150 K, 50 K and 2 K are shown in Figure 4.5(g), Figure 4.5(h), and Figure 4.5(i), respectively. In contrast to the austenite and premartensite phases, the ρ_{xy}^{exp} exhibits hump-like feature around $\pm$1 T and exceeds the ρ_{xy}^{cal} in the martensite phase as clearly visible in Figure 4.5(g) to Figure 4.5(i). The mismatch between ρ_{xy}^{exp} and ρ_{xy}^{cal} in the austenite, premartensite, and martensite phases are anticipating the topological Hall contribution to the ρ_{xy}^{exp} in addition to the ordinary and anomalous Hall contribution [167, 187, 190]. The topological Hall resistivity (ρ_{xy}^{T}) was extracted separately and discussed as below.

The ρ_{xy}^{T} is shown in Figure 4.5(j) and Figure 4.5(k), where Figure 4.5(k) depicts the contour mapping of ρ_{xy}^{T}. The ρ_{xy}^{T} is quite sharp and its maximum value appears at very low field (around $\pm$0.12 T) in the austenite (T = 350 K to 260 K) and premartensite phases (T = 250 K to 200 K), as clearly visible in Figure 4.5(j). In contrast, broad maxima appear in the ρ_{xy}^{T} at relatively higher field (around $\pm$0.9 T) in the martensite phase (T = 150 K to 2 K). It is worth mentioning here that the sign of ρ_{xy}^{T} become reversed in the martensite phase in comparison to the "A+PM" phases. This is probably related to symmetry breaking in the martensite phase, which exhibits higher anisotropy energy [326]. It has been suggested that the spin polarization changes significantly in

the martensite phase in comparison to the austenite phase of Ni_2MnGa [334]. In the austenite phase, the Ni *d* minority-spin (spin-down) electrons play an important role in the density of states (DOS) with the presence of a peak in ultraviolet photoemission (UPS) around 0.3 eV energy, which (peak) disappear in the martensite phase [334]. In contrast, Ni *d* and Mn *d* majority-spin (spin-up) electrons enhanced the DOS around 0.8 eV energy in the martensite phase [334]. Therefore, the present sign reversal of ρ_{xy}^{T} in Ni_2MnGa is attributed to change in the spin polarization of charge carriers (associated with change in electronic structure) with temperature similar to that observed in other well-known skyrmion host systems like MnSi [340].

The absence of any notable difference in the maximum value of ρ_{xy}^{T} between cubic austenite and premartensite phases can be due to preserved cubic austenite phase symmetry in the premartensite phase also [63, 104]. In contrast, a significant change in the maximum value of ρ_{xy}^{T} and magnetic field for the martensite phases is due to the breaking of cubic symmetry (Bain distortion) in the martensite phase (Figure 4.5(j)). For better visualization, the contour mapping of ρ_{xy}^{T} as a function of the magnetic field and temperature is given in Figure 4.5(k), which shows that the magnetic field at which ρ_{xy}^{T} achieve maximum value, is higher in the martensite phase in comparison to the austenite and premartensite phases. Further, the magnitude of the ρ_{xy}^{T} remains nearly temperature independent in the martensite phase (at $T \leq 150$ K). We anticipate that this mismatch appears because of higher MCA energy in the martensite phase in comparison to the austenite and premartensite phases [326].

The skyrmions (stabilized due to geometric confinement of magnetic structure by twin boundaries) in the martensite phase of single-crystalline Ni_2MnGa, has already been reported [11], which affirms the appearance of THE in the martensite phase of present Ni_2MnGa MSMA. Further, the

premartensite phase, which is a precursor phase of the martensite phase [104], has been proposed to be closely linked with zero-field skyrmion formation in the $Ni_{50}Mn_{35.2}In_{14.8}$ MSMA [83], which anticipates the appearance of THE even in the premartensite phase. Moreover, the local (short-range ordered) precursor state of the premartensite phase present in the austenite phase, as reported by a local structural study of Ni_2MnGa MSMA [64], emerges the possibility of THE even in the cubic austenite phase of Ni_2MnGa. Therefore, it is important to investigate the origin of present THE in Ni_2MnGa i.e., whether THE is induced by Berry curvature in the real-space associated with skyrmions [190] or by some noncoplanar spin structure with finite spin chirality [162, 170, 195]. In order to confirm this, the temperature dependence of the maximum value of topological Hall resistivity ($\rho_{xy}^{T_{max}}$) is shown in Figure 4.6(a) wherein green, red, and blue dotted lines indicate the behavior of $\rho_{xy}^{T_{max}}$ in the austenite, premartensite, and martensite phase, respectively. It is evident from Figure 4.6(a) that $\rho_{xy}^{T_{max}}$ remains almost independent with changes in temperature in the martensite and premartensite phases. This behavior is similar to other related Heusler compounds (Mn_2NiGa [165] and $Mn_{1.4}PtSn$ [169]) in which temperature independent $\rho_{xy}^{T_{max}}$ has been shown. This suggests the origin of THE in the martensite and premartensite phases of Ni_2MnGa is induced by real-space Berry curvature accompanied with skyrmions. In contrast, a merely temperature dependent variation of $\rho_{xy}^{T_{max}}$ can be noted in the austenite phase (Figure 4.6(a)). This attributes to the fact that THE may be induced by noncoplanar spin structure with finite spin chirality [162]. This is possibly arises due to the local premartensite phase present in the austenite phase of Ni_2MnGa as reported [64].

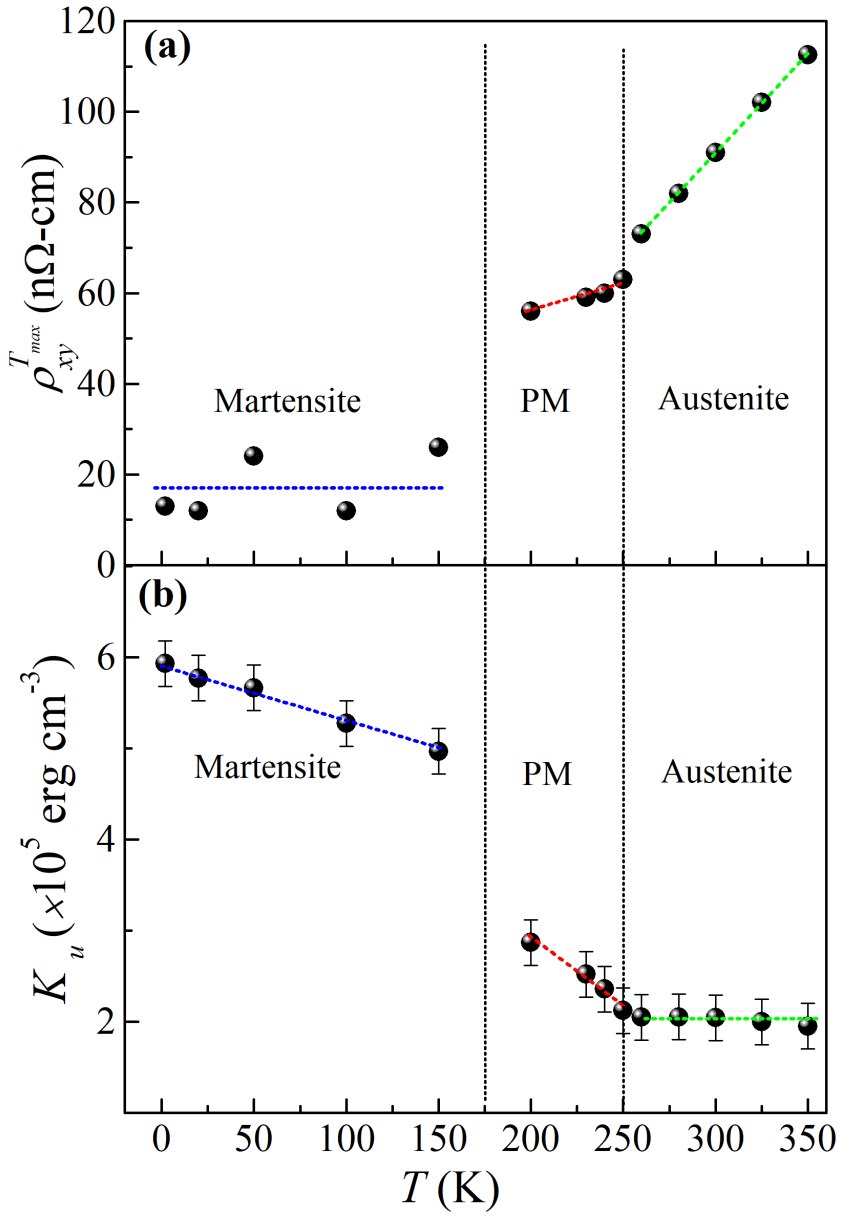

Figure 4.6: Temperature dependence of (a) maximum value magnitude of topological Hall resistivity ($\rho_{xy}^{T_{max}}$) and (b) anisotropy constant (K_u) of Ni_2MnGa. The austenite, premartensite (PM), and martensite phase regions are separated by vertical dashed lines. Green, red and blue color dotted lines are to guide the behavior of $\rho_{xy}^{T_{max}}$ and K_u in the austenite, PM and martensite phases, respectively.

Further, this temperature dependent THE behavior may arise because of change in nucleation probability of noncoplanar spin structure with finite chirality near FM transition temperature T_C [165]. However, a recent study reveals the appearance of THE in $Ni_{47.3}Mn_{30.6}Ga_{22.1}$ thin film specimen and proposed that the origin of ρ_{xy}^{T} is not relate to the skyrmion textures due to negative sign for positive field, very small magnitude and unusual temperature dependent behavior of ρ_{xy}^{T} [149]. In contrast, in the present study, the positive sign of ρ_{xy}^{T} for the positive field in the martensite phase. In addition, significant magnitude and negligible temperature dependency of ρ_{xy}^{T} in the martensite and premartensite phase of Ni_2MnGa are in agreement with other well-known skyrmion host systems [165, 169, 187, 190]. These results confirm the presence of THE is due to topologically protected skyrmion textures in the martensite and premartensite phases of bulk Ni_2MnGa. In general, the signal of $\rho_{xy}^{T_{max}}$ considered as directly proportional to the density of skyrmions and inversely proportional to the size of skyrmions [165]. A significant increase in the nucleation probability of skyrmions around the magnetic phase transition temperature has been reported for the bulk system [165]. The higher value of $\rho_{xy}^{T_{max}}$ in the early premartensite phase (at $T \sim 250$ K) in comparison to low temperature premartensite phase (at $T \sim 200$ K) is anticipated by higher nucleation ability of skyrmions at austenite to premartensite phase boundary [165]. Similarly, the highest value of $\rho_{xy}^{T_{max}}$ in the martensite phase at 150 K is possibly due to higher nucleation ability of skyrmions at premartensite to martensite phase boundary [165].

The positive field value above which the ρ_{xy}^{T} tends to zero is the considered as skyrmions vanishing field (H_C), i.e., the non-trivial spin configuration of skyrmions transforms to collinear FM state above H_C [187]. The $H_C \sim \pm 0.5$ T for the premartensite phases at 230 K, while $H_C \sim \pm 1.5$ T for the martensite phase at 150 K (see Figure 4.5(j)). The larger value of magnetic field ($H_C \sim \pm 1.5$ T)

to vanish the skyrmion textures for the martensite phase in comparison to the premartensite phase ($H_C \sim \pm 0.5$ T) manifest the more stable skyrmion textures in the martensite phase. This can be understood by the higher value of MCA energy in the martensite phase in comparison to the premartensite phase [263, 326], i.e., sufficient high MCA energy is present to form stable skyrmion textures in the martensite phase. This means MCA plays a key role in the stabilization of magnetic skyrmions, which forms due to competing interactions between magnetic anisotropy energy and dipolar interactions in centrosymmetric systems like Ni_2MnGa; therefore, it is important to investigate the MCA in Ni_2MnGa. The value of the magnetic anisotropy constant (K_u) was obtained using the law of saturation method [341]. The high field *M(H)* were employed for least-squares fitting using equation $M = M_S\left(1 - \frac{4}{15}\frac{K_u}{M_S^2 H^2}\right) + \chi H$, where M_S, K_u, χ are spontaneous magnetization, anisotropy constant, and ac-susceptibility, respectively [341]. The obtained value of K_u is shown in Figure 4.6(b). On lowering the temperature, however, K_u remains almost constant in the austenite phase; a small increasing trend is observed in the premartensite phase. In contrast, K_u increases drastically into the martensite phase due to the formation of the martensite twin variant with different orientations. The present behavior of K_u in different phases appeared as expected for the Ni_2MnGa [263, 326]. It is worth mentioning here that the drastic increase in K_u favors the formation of stable skyrmion textures in the martensite phase compared to the premartensite phase.

4.4 Conclusions

In conclusion, the observation of AHE and THE in the bulk Ni_2MnGa MSMA are presented. The magnetization and resistivity reveal the structural and magnetic phase transitions. The net change in magnitude of the negative MR with the magnetic field is decreased on decreasing temperature and explained by the *s-d* scattering model. The detailed scaling study of anomalous Hall conductivity reveals that the intrinsic Berry phase contribution dominates in all phases (austenite,

premartensite, and martensite phases). The evidence for the THE observed in the FM austenite, premartensite, and martensite phases, whereas THE vanishes above FM T_C. The magnitude and temperature independent behavior of maximum value of topological Hall resistivity attributed to the appearance of THE induced by real-space Berry curvature associated with topological protected magnetic skyrmions in the martensite and premartensite phases of Ni_2MnGa. The present findings open a new pathway in the centrosymmetric skyrmion host systems that exhibit magnetic shape memory effect.